SET domain containing 2 (SETD2) influences metabolism and alternative splicing during myogenesis

Hannah J. Wiedner[1,2] (iD), Eduardo V. Torres[1] (iD), R. Eric Blue[1] (iD), Yi-Hsuan Tsai[3], Joel Parker[2,3] and Jimena Giudice[1,2,4] (iD)

1 Department of Cell Biology and Physiology, The University of North Carolina at Chapel Hill, USA
2 Curriculum in Genetics and Molecular Biology (GMB), The University of North Carolina at Chapel Hill, USA
3 Lineberger Comprehensive Cancer Center, The University of North Carolina at Chapel Hill, USA
4 McAllister Heart Institute, School of Medicine, The University of North Carolina at Chapel Hill, USA

Epigenetic regulatory mechanisms are increasingly recognized as crucial determinants of cellular specification and differentiation. During muscle cell differentiation (myogenesis), extensive remodelling of histone acetylation and methylation occurs. Several of these histone modifications aid in the expression of muscle-specific genes and the silencing of genes that block lineage commitment. Therefore, the identification of new epigenetic regulatory mechanisms is of high interest. Still, the functional relevance of numerous histone modifications during myogenesis remain completely uncertain. In this study, we focus on the function of H3K36me3 and its epigenetic writer, SET domain containing 2 (SETD2), in the context of muscle cell differentiation. We first observed that SETD2 expression increases during myogenesis. Targeted depletion of SETD2 in undifferentiated (myoblasts) and differentiated (myotubes) muscle cells reduced H3K36me3 levels and induced profound changes in gene expression and slight alterations in alternative splicing, as determined by deep RNA-sequencing analysis. Enzymes that function in metabolic pathways were upregulated in response to SETD2 depletion. Furthermore, we demonstrated that upregulation of several glycolytic enzymes was associated with an increase in intracellular pyruvate levels in SETD2-depleted cells, indicating a novel role for SETD2 in metabolic programming during myogenesis. Together, our results provide new insight into the signalling pathways controlled by chromatin-modifying enzymes and their associated histone modifications during muscle cell differentiation.

Introduction

During cellular differentiation, extensive changes in gene expression occur. These transcriptional changes coincide with, and are sometimes regulated by, chromatin alterations at the same loci. Loss of function mutations in histone reader, writer, and eraser enzymes are common in developmental diseases and cancer, suggesting that these proteins, and the chromatin marks they modify, aid in regulating gene expression during cellular differentiation and the maintenance of tissue homeostasis [1].

The skeletal muscle cell differentiation program (myogenesis) is highly regulated by a combination of extracellular signals, transcriptional factors, microRNAs (miRNAs), and chromatin remodelling enzymes [2,3]. Six homeobox 1 and 4 (SIX1 and SIX4) and paired box 3 and 7 (PAX3 and PAX7) are major transcription factors that regulate specification and commitment of early myogenic progenitor cells [4,5]. As differentiation progresses, SIX1, SIX4, PAX3, and PAX7 are repressed as the expression of myogenic regulatory factors including myogenic differentiation 1 (MYOD1), myogenic factor 5 (MYF5), and myogenin (MYOG) is activated. Myogenic regulatory factors bind to E box motifs, which are found at the promoters or enhancers of muscle-specific genes to increase their expression [6,7]. In part, PAX3 and PAX7 repression is achieved through MYOD1-mediated activation of miR206 that targets PAX3 and PAX7 for degradation, thereby pushing cells towards terminal differentiation [8,9].

Epigenetic writing enzymes can operate in concert with these transcription factors to mediate multiple stages of myogenesis. In muscle precursor cells, MYOD1 associates with the histone deacetylase 1 (HDAC1) to inhibit expression of muscle-specific genes [10]. Myogenic differentiation is then dependent on a switch between the association of MYOD1 and HDAC1 in undifferentiated cells to MYOD1 and the lysine acetyltransferase 2B (KAT2B also known as P/CAF) [10,11] in differentiated cells. The interaction between MYOD1 and KATB2 stimulates gene expression programs leading to terminal differentiation [11]. In fact, genome-wide studies indicate that MYOD1 frequently localizes to areas of histone acetylation in skeletal muscle cells [12]. Globally, histone acetylation levels decrease during the differentiation of mouse C2C12 myoblasts and muscle stem cells in culture [13,14]. In muscle stem cells, this switch is driven by increased glucose utilization that reduces histone acetylation at genes that must be silenced for differentiation to proceed [14].

Histone methylation can also activate or repress myogenic gene expression programs. During lineage commitment, PAX7 stimulates MYF5 expression by remodelling nearby H3K4 tri-methylation (H3K4me3) through its association with the WDR4-ASH2L-MLL2 histone methyltransferase (HMT) complex [15]. PAX7 is also silenced through the deposition of H3K27 tri-methylation (H3K27me3) at its promoter by the enhancer of the zeste 2 polycomb repressive complex 2 subunit (EZH2) [16]. In addition, EZH2 inhibits the expression of MYOG until the initiation of differentiation when the lysine demethylase 6A (KDM6A) is recruited to erase H3K27me3 which, in turn, allows myogenesis to proceed [17,18]. Derepression of MYOG is further accomplished by demethylation of H3K9 di- and tri-methylation (H3K9me2 and H3K9me3) by the lysine demethylase 4A/C (KDM4A/C) which is required for muscle cell differentiation [19]. While these studies have demonstrated the importance of posttranslational acetylation, H3K4me3, H3K27me3, H3K9me2, and H3K9me3 to the myogenic gene expression program, the function of other chromatin marks, and their epigenetic writers, remain unclear.

SET domain containing 2 (SETD2) is the only histone methyltransferase known to tri-methylate H3K36me (H3K36me3) [20]. SETD2 associates with the RNA polymerase II during transcriptional elongation to deposit H3K36me3 on actively transcribed genes [21–24]. H3K36me3 deposition is not only a consequence of transcription but also functions to recruit deacetylases or methyltransferases which inhibit transcriptional initiation at cryptic sites and promote transcriptional fidelity [25–28]. In cell culture systems and *in vivo*, H3K36me3 recruits RNA-binding proteins to nascent RNA, thereby altering constitutive and alternative splicing decisions co-transcriptionally [24,29–31]. Knockout of *Setd2* results in embryonic lethality in mice and produces defects in vascular remodelling prior to death [32]. Although SETD2 functional studies in muscle are limited, *Setd2*$^{-/-}$ myoblasts are unable to differentiate and have reduced proliferative capacity, due to decreased expression of genes involved in cell-cycle regulation [33]. Genome-wide analyses indicate that histone marks, including H3K36me3, are remodelled during myogenesis [13]. These studies suggest that SETD2 is important during myogenesis, possibly through regulating gene expression and splicing programs, but the affected pathways have not yet been determined in an unbiased, genome-wide manner.

Here, we investigate how H3K36me3 and its epigenetic writer, SETD2, influence transcriptional and posttranscriptional programs during myogenesis using deep RNA-sequencing. Our results indicate that SETD2 functions to regulate metabolic programs and to fine-tune splicing patterns.

Results

SETD2 expression increases during myogenesis

Differentiation of mouse C2C12 myoblasts into myotubes is a robust, well-described, and established model of myogenesis [34,35]. Reduction of serum concentration in culture induces the fusion of mononucleated myoblasts into multinucleated myotubes that share characteristics with early skeletal muscle fibres (Fig. 1A). C2C12 cell differentiation recapitulates the extensive transitions in gene expression and alternative splicing programs occurring in early skeletal muscle development *in vivo* [36–39]. Therefore, this is a suitable system to investigate the role of SETD2 in transcriptional and posttranscriptional programs in the context of muscle. We first evaluated the expression level of myosin heavy chain (MYH), a well-established myogenic marker, during C2C12 cell differentiation. MYH levels greatly increase upon the induction of differentiation, illustrating that the cells were efficiently differentiated (Fig. 1B). We next examined the expression of SETD2 and H3K36me3 over the course of 6 days of myoblast differentiation to myotubes. We found a significant, approxmately 2-fold increase in SETD2 expression, but no change in H3K36me3 levels during myogenesis (Fig. 1B–D).

Depletion of SETD2 in myoblasts and myotubes reduces total H3K36me3

To carefully examine the role of SETD2 during myogenesis, we performed targeted depletion of SETD2 using two independent small interfering RNAs

(si-RNAs) in myoblasts. Myoblasts were either harvested 24 h after depletion or differentiated for 96 h into myotubes before being subjected to deep RNA-sequencing analysis (Fig. 2A). Western blot analysis indicated that si-Setd2 treatment reduced SETD2 expression by 98% and 88% in myoblasts and myotubes, respectively (as determined by the mean of si-Setd2 #1 and si-Setd2 #2). Similarly, we observed a 70% and 67% decrease in H3K36me3 in transfected myoblasts (Fig. 2B) and myotubes (Fig. 2C) compared to a nontargeting si-RNA (si-Ctrl). Therefore, both SETD2 and H3K36me3 levels were strongly decreased by both si-Setd2 #1 and si-Setd2 #2 treatment. Messenger RNAs (mRNAs) were then captured using magnetic oligo-dT beads and cDNA libraries were analysed using an Illumina NovaSeq6000 instrument with > 60 million read pairs per sample. All samples had a high degree of sequencing accuracy, with > 90% of read pairs mapping to the mouse genome (Table S1).

Depletion of SETD2 and H3K36me3 produced no visually observable defects in myoblast morphology or myotube differentiation as determined by light microscopy and immunofluorescence confocal microscopy (Fig. 3A–C). Quantification of fusion index, a widely-used measure of the degree of cell–cell fusion and muscle cell differentiation [40,41], were similar among control and SETD2-depleted myotubes (Fig. 3D). The total number of nuclei within each field of view was unaffected by SETD2 depletion, as determined by DAPI staining (Fig. 3E). Furthermore, the expression levels of myogenenic markers such as MYH, the myogenic differentiation 1 (MYOD1), and myogenin (MYOG) were unchanged in si-Setd2 treated myotubes
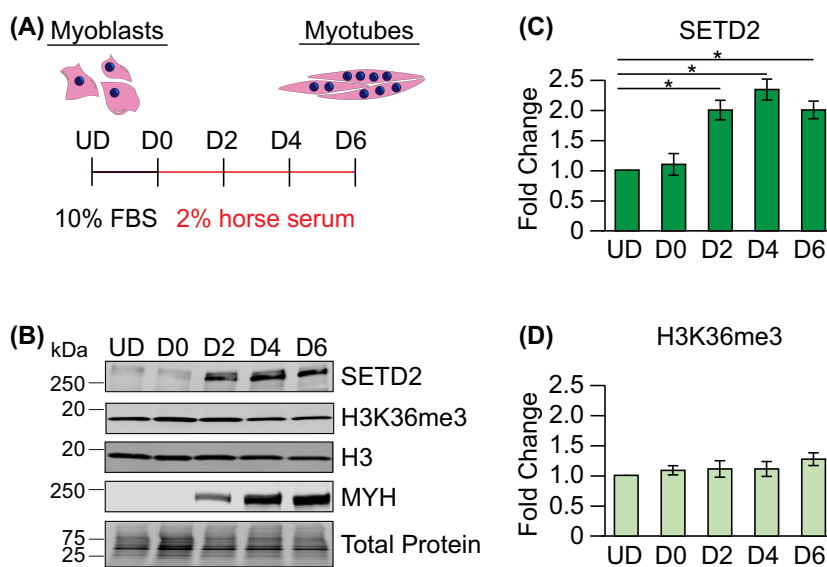
Fig. 1. SETD2 expression is regulated during myogenesis. (A) Schematic of myoblast differentiation into myotubes in culture. (B–D) SETD2 expression and H3K36me3 levels during myoblast differentiation into myotubes were determined by western blot assays (*n* = 4). Myosin heavy chain (MYH) expression was used to monitor efficient C2C12 cell differentiation. FBS, fetal bovine serum; UD, undifferentiated; H3, histone 3. *P < 0.05 (versus undifferentiated cells), Student *T* test.
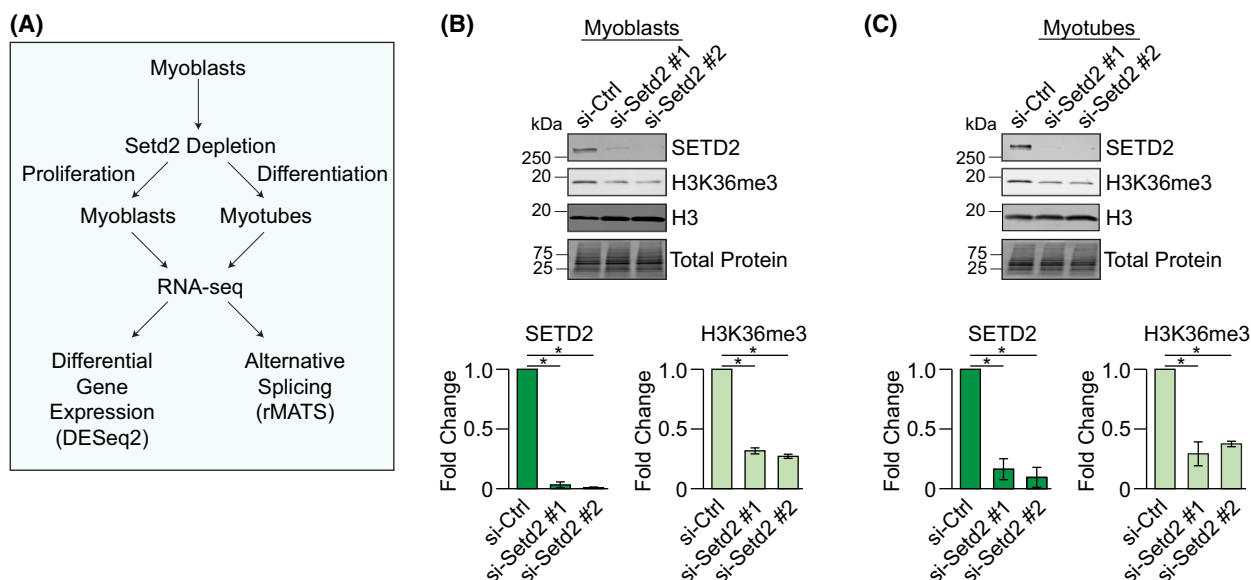
Fig. 2. Myoblasts and myotubes were depleted of SETD2 before being subjected to RNA-sequencing. (A) Schematic of experimental strategy for RNA-sequencing analysis (*n* = 3). (B, C) SETD2 and H3K36me3 levels were measured in myoblasts (B) and myotubes (C) by western blotting following si-Setd2 delivery (*n* = 3). H3, Histone 3. *P < 0.05 (versus si-Ctrl), Student *T* test.

(Fig. 3F–I). These data suggest that any detected changes in gene expression and alternative splicing are likely to be caused by SETD2 depletion, and not simply the result of defects in differentiation or low cell viability.

H3K36me3 fine-tunes splicing patterns in myoblasts and myotubes

We detected 108 and 162 splicing events that were significantly different from the controls in both si-Setd2 #1 and si-Setd2 #2 treated myoblasts and myotubes, respectively (Fig. 4A and File S1). Differences in percent spliced in (ΔPSI) values (defined as the difference between the PSI in control cells and the PSI in si-Setd2 treated cells, i.e. si-Ctrl – si-Setd2) were highly correlated between the two si-RNAs in myoblasts (Pearson = 0.93) and myotubes (Pearson = 0.89; Fig. 4 B), demonstrating a high degree of reproducibility of our findings among different si-RNAs. Both in myoblasts and myotubes, over 50% (52% in myoblasts and 56% in myotubes) of the differential splicing events had a |PSI| < 20% (Fig. 4B, red dots), suggesting that H3K36me3 primarily fine-tunes splicing patterns in muscle cells. Gene ontology (GO) analysis of all of the differentially spliced genes in both si-Setd2 conditions was performed using ENRICHR [42–44]. We observed an overrepresentation of splicing events in

genes encoding proteins involved in DNA damage response and muscle contraction in myoblasts and myotubes, respectively (Fig. 4C,D).

RNA-sequencing data were next visualized using the UCSC genome browser and validated by reverse transcription PCR (RT-PCR) using primers designed to hybridize with the constitutive exons flanking the alternative regions (Fig. 5A–L). PSI values were calculated by densitometry and the ΔPSI values for 12 splicing events from RT-PCR experiments were correlated with those obtained from the RNA-sequencing studies (Fig. 5M). The ΔPSI values calculated from RT-PCR assays were highly correlated (Pearson = 0.96) with ΔPSI values determined by computational analysis of RNA-sequencing data, indicating robust detection of splicing events.

Alternative splicing events were categorized into five major types, based on the location of the alternative region: cassette exon (CE), retained intron (RI), alternative 3′ splice site (A3SS), alternative 5′ splice site (A5SS), or mutually exclusive exon (MXE) (Fig. 6A,B). The most common type of alternative splicing event detected after SETD2 depletion in both myoblasts and myotubes were those occurring in cassette exons (58% of events in myoblasts and 62% in myotubes; Fig. 6B). We found an approximately equal number of events where the alternative region was more included or more excluded in response to SETD2 depletion both in myoblasts and
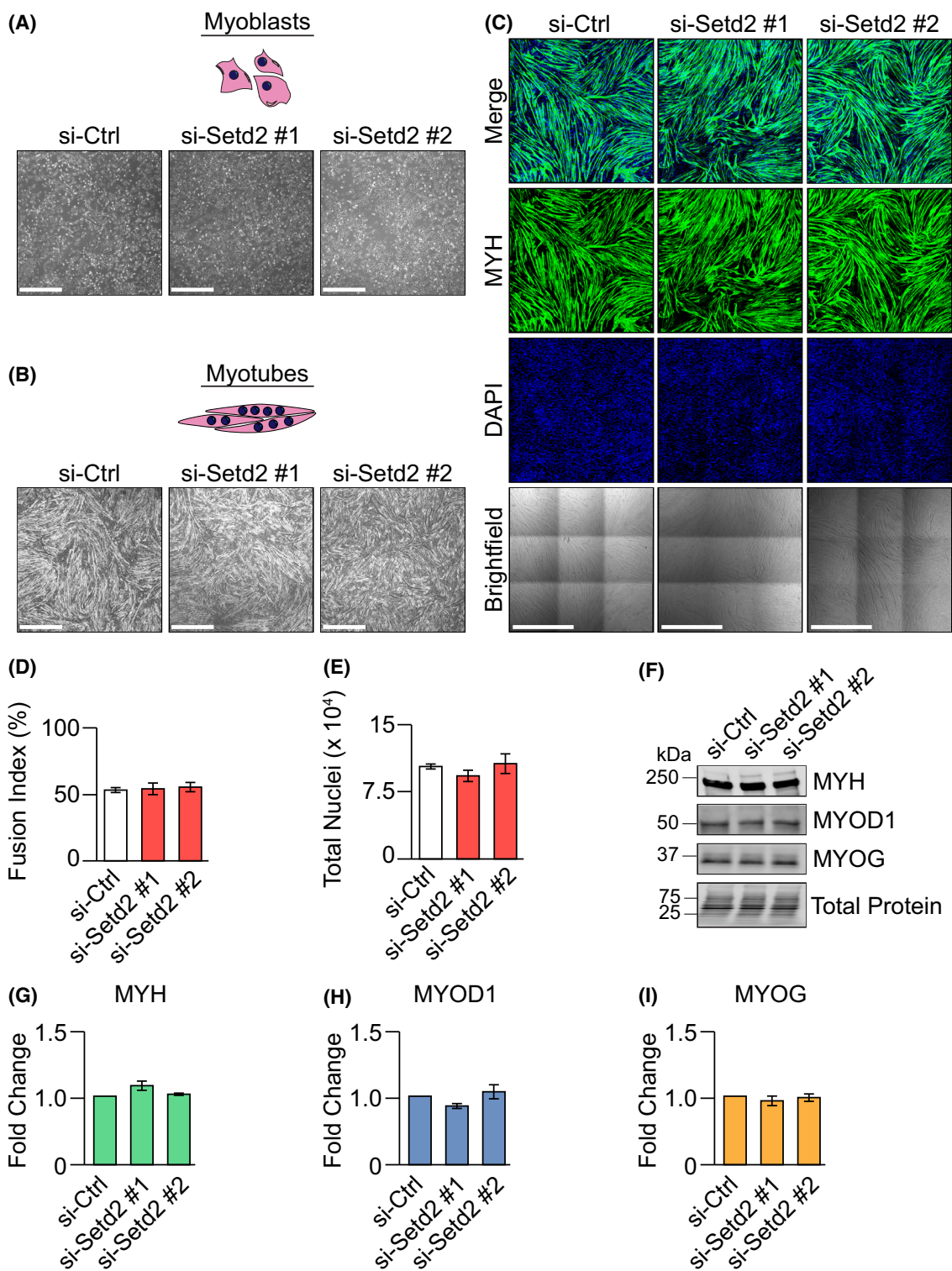
Fig. 3. si-Setd2 treatment does not affect muscle cell differentiation. (A, B) Light microscopy analysis of myoblasts and myotubes after SETD2 depletion. (C) Immunofluorescence confocal microscopy staining of myosin heavy chain (MYH) in SETD2-depleted myotubes. (D, E) Fusion index (D) and total nuclei (E) were determined by microscopy image analysis (*n* = 3). (F–I) Expression of MYH (G), myogenic differentiation 1 (MYOD1) (H), and myogenin (MYOG) (I), in SETD2-depleted myotubes was determined by western blot assays (*n* = 4). Scale bars = 1 mm.

(A)

Myoblasts

si-Setd2 #1   si-Setd2 #2

299   108   588

$p < 2e\text{-}16$

Myotubes

si-Setd2 #1   si-Setd2 #2

423   162   655

$p < 2e\text{-}16$

(B)

Pearson = 0.93
$p = 1e\text{-}60$
$n = 108$ events

ΔPSI si-Setd2 #2

100

0

-100

-100   0   100

n = 56 (52%)

ΔPSI si-Setd2 #1

Pearson = 0.89
$p = 2.7e\text{-}57$
$n = 162$ events

ΔPSI si-Setd2 #2

100

0

-100

-100   0   100

n = 91 (56%)

ΔPSI si-Setd2 #1

(C)

Myoblasts

negative regulation of response to DNA damage
replication fork processing
endosome organization
regulation of DNA recombination
DNA replication maintenance of fidelity
regulation of DNA metabolic process
regulation of lamellipodium organization
cartilage development
regulation of isotype switching
epiboly involved in wound healing

$p = 0.05$

0   2   4

-log p

(D)

Myotubes

actin-myosin filament sliding
muscle filament sliding
muscle contraction
negative regulation of junction assembly
synaptic vesicle docking
negative regulation of metabolic process
positive regulation of muscle contraction
muscle cell development
positive regulation of secretion by cell
actomyosin structure organization
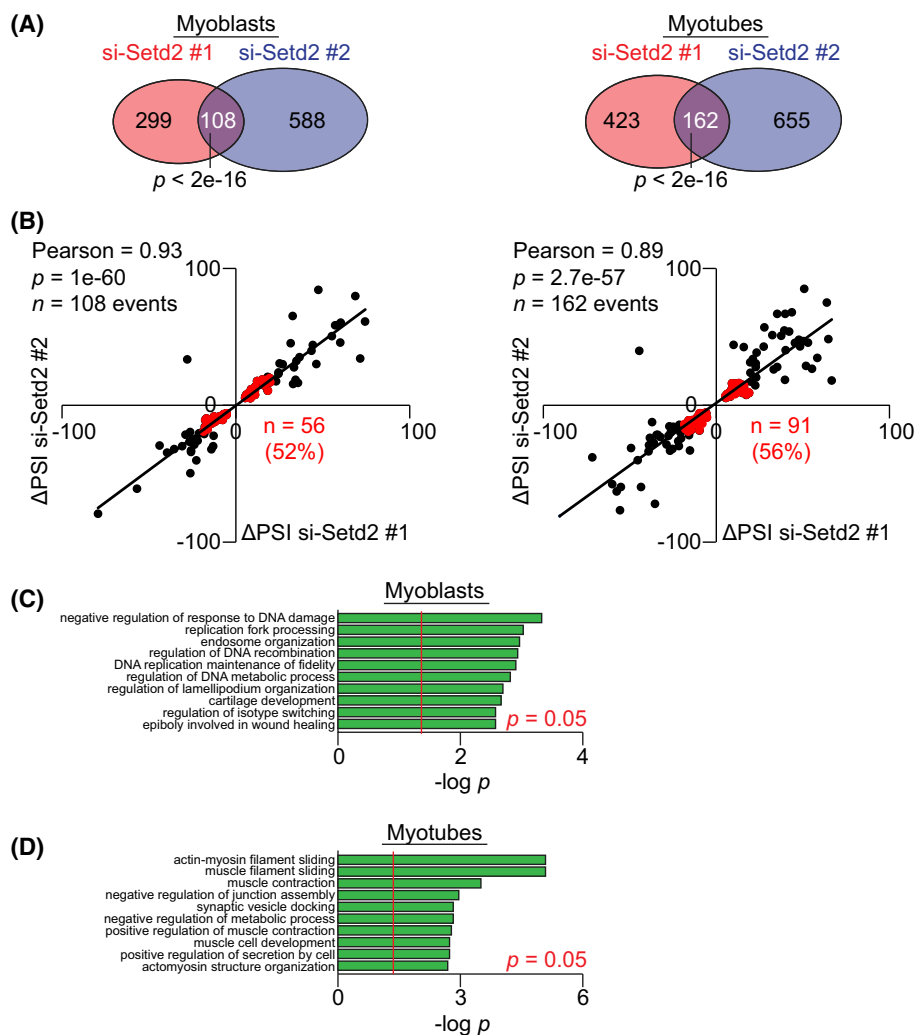
$p = 0.05$

0   3   6

-log p

Fig. 4. SETD2 fine-tunes splicing patterns in myoblasts and myotubes. (A) Venn diagrams displaying the overlap between alternative splicing changes in myoblasts (left) and myotubes (right) after treatment with si-Setd2 #1 or si-Setd #2 or a control si-RNA (si-Ctrl). (B) Correlation plot between the ΔPSI for si-Setd2 #1 and si-Setd2 #2 obtained by RNA-sequencing in myoblasts (left) and myotubes (right). ΔPSI was defined as the difference between the PSI in SETD2-depleted cells and the PSI in control cells. Events with IΔPSII < 20% are shown in red. (C, D) Gene ontology analysis (biological process) of differentially spliced genes in si-Setd2 #1 and si-Setd2 #2 treated myoblasts (C) and myotubes (D). Red line indicates $P = 0.05$. PSI, percent spliced in. *P*-values were determined by Fisher's exact test (A, C, D), or significance test for correlation, based on a *T* distribution (B).

myotubes (Fig. 6C), indicating that H3K36me3 can either activate or repress inclusion of alternative regions.

In several instances, multiple differential splicing events were detected in a single gene. In total, differential alternative splicing events occurred in 103 genes (108 total splicing events) in myoblasts and in 140 genes (162 total splicing events) in myotubes. We next asked whether the same genes that were alternatively spliced in response to SETD2 depletion were also differentially expressed. We observed very little overlap between genes regulated by alternative splicing and those that change in their overall expression level

(FC > 1.25, which means FC > 1.25 for upregulation or FC < 1/1.25 for downregulation, *P-adj* < 0.05; Fig. 6D). These results indicate that differences in total gene expression are not driven by changes in alternative splicing patterns (through nonsense mediated decay, for example) in SETD2-depleted cells.

SETD2 controls extensive gene expression programs in myoblasts and myotubes

Analysis of RNA-sequencing data revealed extensive changes in gene expression programs both in
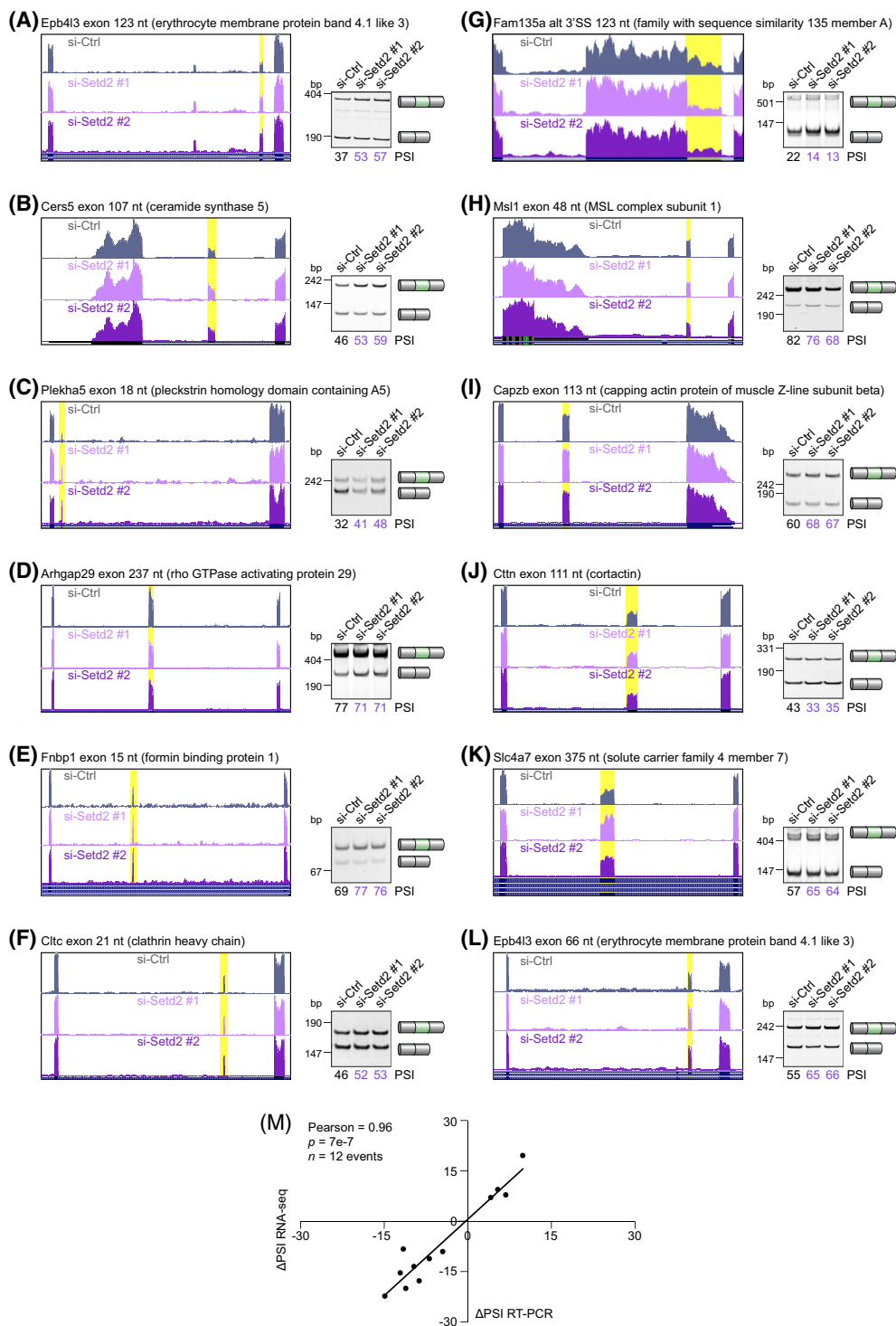
Fig. 5. Differential splicing events detected by RNA-seq are validated by RT-PCR assays. (A–L) Validation of splicing changes determined by RNA-sequencing and those measured from RT-PCR assays in SETD2 depleted cells. RNA-sequencing tracks (UCSC browser – mm10, left) and RT-PCR assays (right) for differentially spliced genes. (M) The correlation between ΔPSI values from RNA-sequencing (RNA-seq) and ΔPSI values from RT-PCR is shown. bp, basepairs; nt, nucleotides; PSI, percent spliced in. *P*-values were determined by significance test for correlation, based on a *T* distribution (M).
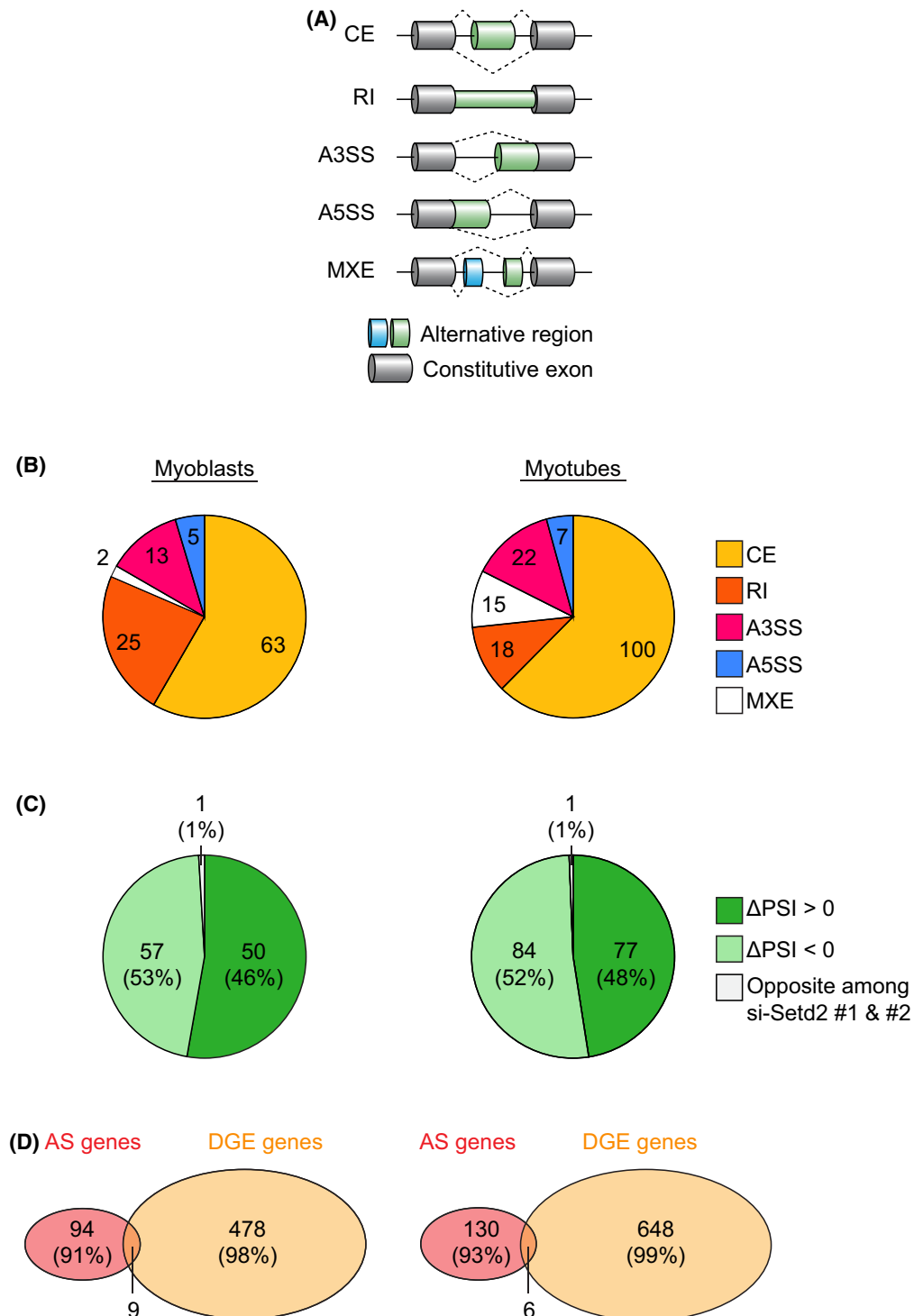
Fig. 6. SETD2 can either activate or repress inclusion of alternative regions. (A) Schematic displaying the five different types of alternative splicing events: cassette exon (CE), retained intron (RI). alternative 3′ splice site (A3SS), alternative 5′ splice site (A5SS), and mutually exclusive exons (MXE). (B) Number of alternative splicing events in response to SETD2 depletion classified based on the type of splicing event in myoblasts (left) and myotubes (right). (C) Splicing events classified based on the direction of the change in response to SETD2 depletion in myoblasts (left) and myotubes (right). ΔPSI < 0 signifies more inclusion in SETD2 depleted cells than in control cells. ΔPSI > 0 signifies more skipping in SETD2 depleted cells than in control cells. (D) Venn diagrams displaying the overlap between alternative splicing changes and differential gene expression (DGE) in myoblasts (left) and myotubes (right). PSI, percent spliced in.
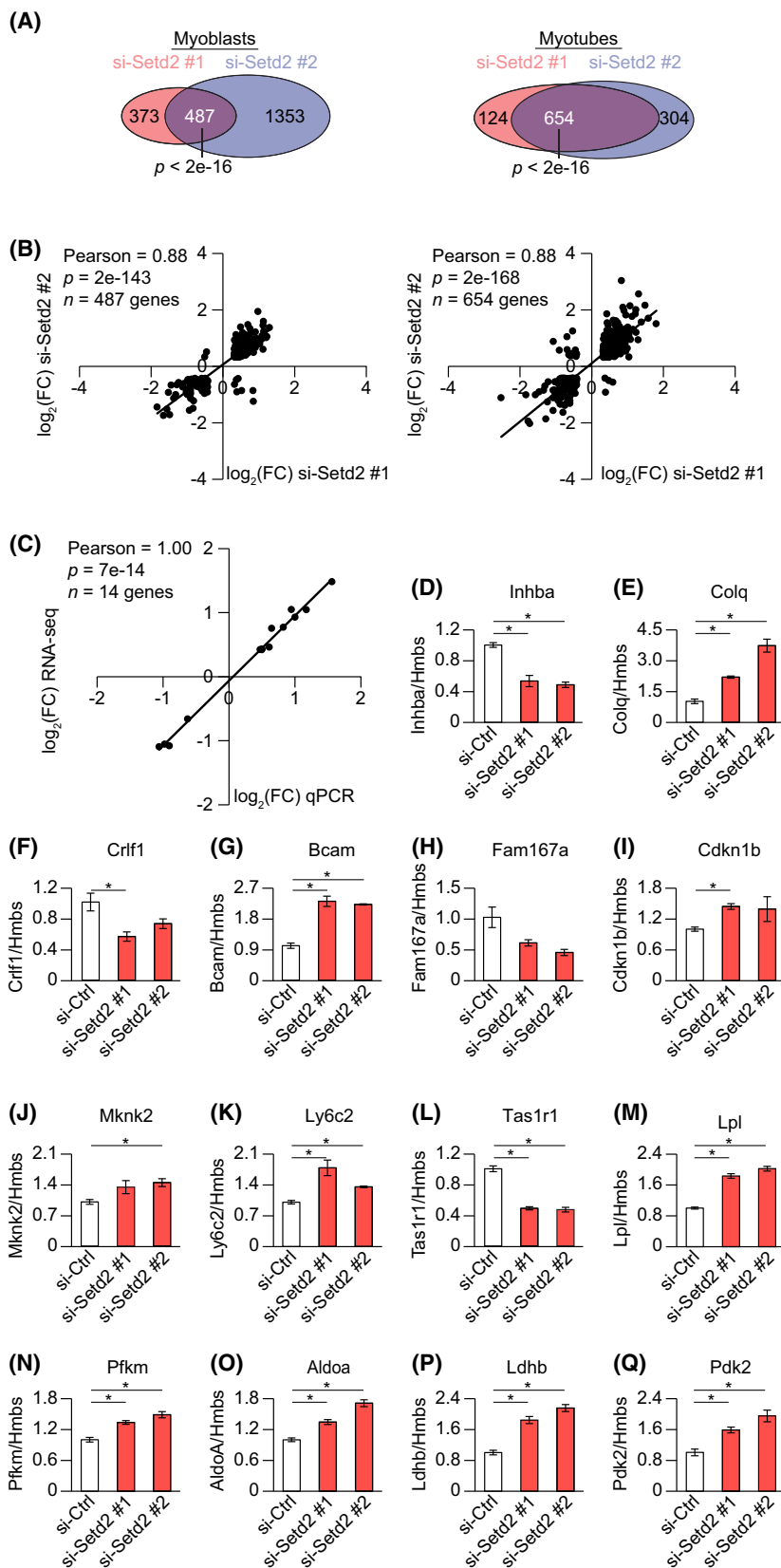
Fig. 7. SETD2 regulates gene expression in myoblasts and myotubes. (A) Venn diagrams displaying the overlap between gene expression changes in SETD2-depleted myoblasts (left) and myotubes (right). (B) Correlation plot between the $\log_2$ fold change (FC) for si-Setd2 #1 and si-Setd2 #2 obtained by RNA-sequencing (RNA-seq) in myoblasts (left) and myotubes (right). (C) The correlation between RNA-sequencing (RNA-seq) and real-time quantitative PCR (qPCR) values is shown. (D–Q) qPCR analysis ($n = 3$) of differentially expressed genes at the transcript level upon SETD2 depletion. Inhba, inhibin subunit beta (D). Colq, collagen-like tail subunit of asymmetric acetylcholinesterase I (E). Crlf1, cytokine receptor like factor 1 (F). Bcam, basal cell adhesion molecule (G). Fam167a, family with sequence similarity 167 member (H). Cdkn1b, cyclin-dependent kinase inhibitor 1B (I). (G) Mknk2, MAPK-interacting serine/threonine kinase 2 (J). Ly6c2, lymphocyte antigen 6c2 (K). Tas1r1, taste 1 receptor member 1 (L). Lpl, lipoprotein lipase (M). Pfkm, phosphofructokinase (N). Aldoa, aldolase fructose-bisphosphate A (O). Ldhb, lactate dehydrogenase B (P). Pdk2, pyruvate dehydrogenase kinase 2 (Q). *$P < 0.05$, Fisher's exact test (A), significance test for correlation (B, C), or Student T test (D–Q) (versus si-Ctrl).

myoblasts and myotubes with significant overlap between si-Setd2 #1 and si-Setd2 #2 (FC > 1.25, *P-adj* < 0.05; Fig. 7A and File S1). Fold changes in gene expression were highly correlated among si-Setd2 #1 and si-Setd2 #2 treated myoblasts (Pearson = 0.88) and myotubes (Pearson = 0.88; Fig. 7B). Differential gene expression analysis was validated by real-time quantitative PCR (qPCR) of 14 genes, which displayed a high degree of correlation with RNA-sequencing data (Pearson = 1.00; Fig. 7C–Q). The strong concordance among si-Setd2 #1 and si-Setd2 #2-treated cells and qPCR assays indicates high accuracy of our differential gene expression analysis.

SETD2 regulates the expression of metabolism-related genes in myotubes

The majority of the differentially expressed genes were upregulated in SETD2-depleted myoblasts and downregulated in SETD2-depleted myotubes (Fig. 8A). Indeed, previous reports demonstrated that SETD2 can repress or promote expression at different loci [45,46]. Next, we performed gene ontology (GO) analysis of all of the differentially expressed genes (FC > 1.25, *P-adj* < 0.05) in both si-Setd2 conditions using ENRICHR [42–44]. Genes encoding proteins involved in cellular differentiation and mitotic spindle organization
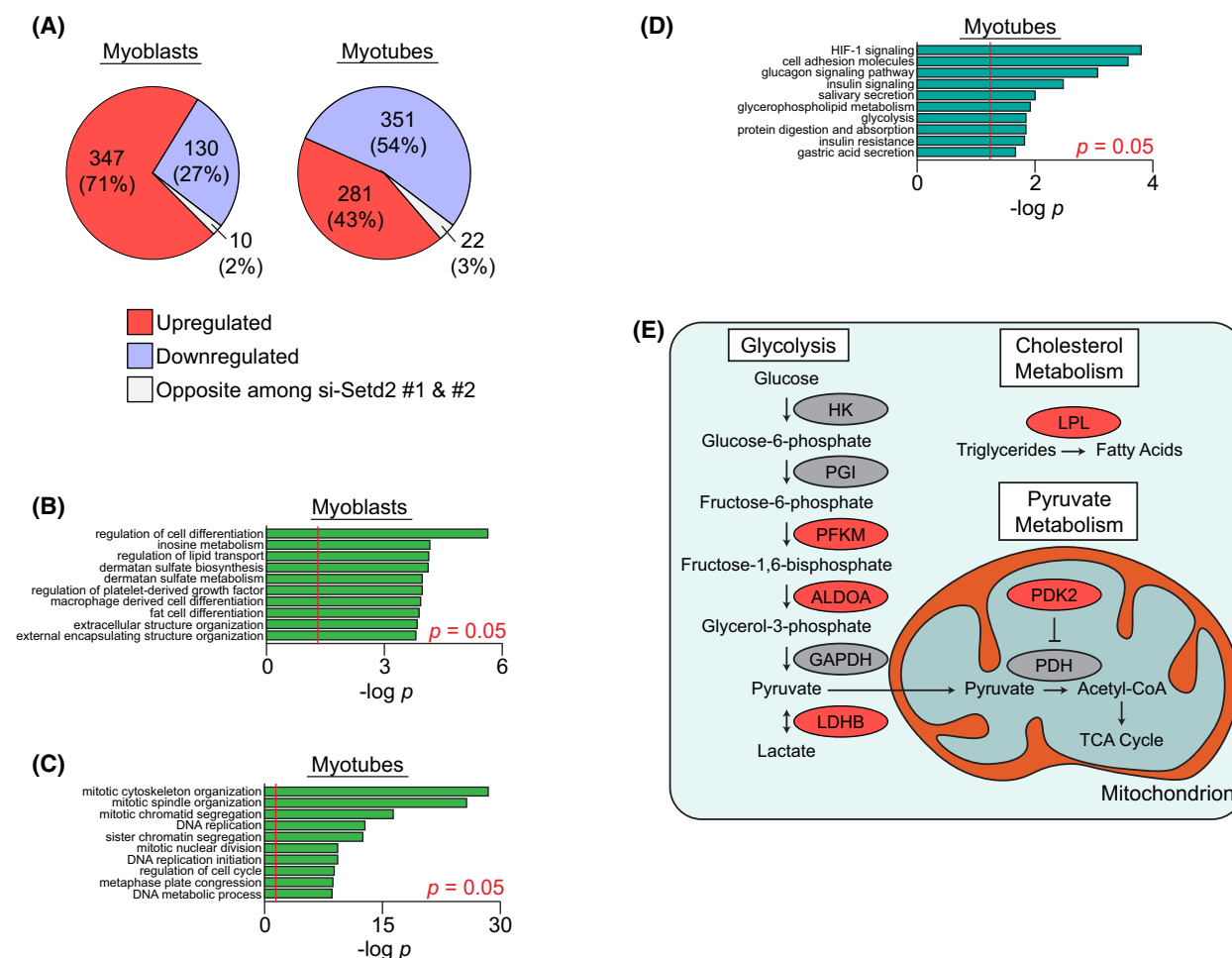

Fig. 8. Metabolism-related genes are upregulated in SETD2-depleted myotubes. (A) Differentially expressed genes classified based on whether they are upregulated in both si-Setd2 #1 & si-Setd2 #2 (upregulated), downregulated in both si-Setd2 #1 & si-Setd2 #2 (downregulated), or regulated in opposite directions in si-Setd2 #1 & si-Setd2 #2 (opposite among si-Setd2 #1 & si-Setd2 #2) in myoblasts (left) and myotubes (right). (B,C) Gene ontology analysis (biological process) of differentially expressed genes in si-Setd2 #1 and si-Setd2 #2-treated myoblasts (B) and myotubes (C). Red line indicates $P = 0.05$. (D) Gene ontology analysis (KEGG pathways) of upregulated genes in SETD2-depleted myotubes. Red line indicates $P = 0.05$. (E) Scheme of cellular metabolic reactions based on glycolysis, cholesterol metabolism and pyruvate metabolism KEGG pathways. Upregulated genes after SETD2 depletion are shown in red. *$P < 0.05$, Fisher's exact test (B–D).

were overrepresented in myoblasts and myotubes, respectively (Fig. 8B,C).

KEGG pathway analysis of upregulated genes in myotubes revealed an enrichment of genes that function in metabolic-related pathways (Fig. 8D). Further inspection of these genes revealed that they encode key enzymes involve in glycolysis, cholesterol metabolism, and pyruvate metabolism (Fig. 8E). As examples, we confirmed by qPCR analysis the upregulation of lipoprotein lipase (Lpl), phosphofructokinase (Pfkm), aldolase fructose-bisphosphate A (Aldoa), lactate dehydrogenase B (Ldhb), and pyruvate dehydrogenase kinase 2 (Pdk2) mRNAs in SETD2-depleted myotubes (Fig. 7M–Q).

In myotubes, SETD2 depletion increases intracellular pyruvate concentration

To determine if SETD2 depletion leads to upregulation of metabolic enzymes at the protein level, we performed western blot assays for PFK1, ALDOA, PDK2, and LDHB (Fig. 9A). Indeed, we observed overexpression of these metabolic proteins (Fig. 9B–E). Because PFK1, ALDOA, PDK2, and LDHB can positively regulate pyruvate levels (Fig. 8E), we hypothesized that intracellular pyruvate concentration could be affected by SETD2 depletion. We directly measured intracellular pyruvate levels in SETD2-depleted myotubes and found an increase in pyruvate concentration compared to control cells (si-Ctrl; Fig. 9

F). These results indicate that SETD2 loss can result in metabolic dysregulation during myogenesis.

Discussion

Previous analyses of the positioning of histone post-translational modifications by chromatin immunoprecipitation sequencing (ChIP-sequencing) revealed that H3K36me3 is preferentially located on exons compared to introns and is believed to be deposited co-transcriptionally by the association between SETD2 and RNA polymerase II [21–24]. Although SETD2 has been mechanistically linked to alternative splicing through the coupling of H3K36me3 and various RNA-binding proteins, we detected relatively minor effects of SETD2 loss on splicing patterns during myogenesis [24,29–31]. One explanation for this finding is that H3K36me3 regulation of splicing may depend on the cell type or tissue context. To date, a connection between H3K36me3 and splicing has been described in epithelial cells, fibroblasts, yeast cells, and even *in vivo* in mouse brains during cocaine addiction and *Arabidopsis thaliana* in response to temperature fluctuations [29–31,47,48]. Still, our study indicates that the dependency of alternative splicing on H3K36me3 in muscle cells is less pronounced. Perhaps this is due to the presence of splicing factors that are known to robustly regulate splicing during myogenesis such as the RNA binding fox-1 homologue 2 (RBFOX2), the muscle-blind like proteins 1 and 2 (MBNL1 and
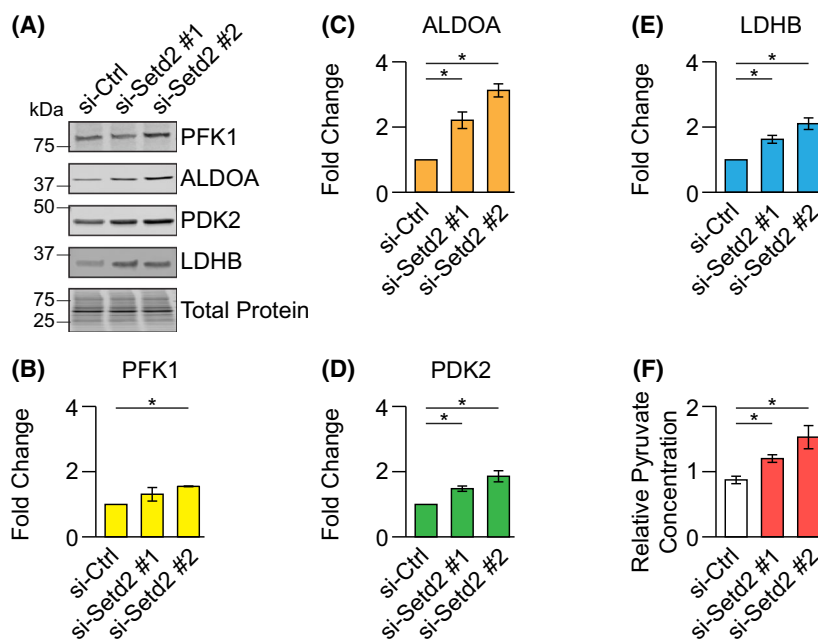

Fig. 9. SETD2 depletion increases expression of glycolytic enzymes and pyruvate concentration. (A–E) Expression of PFK1 (B), ALDOA (C), PDK2 (D), and LDHB (E) were determined by western blot assays in SETD2-depleted myotubes ($n = 3$). (F) Intracellular pyruvate concentration was determined in si-Ctrl and si-Setd2-treated myotubes and normalized to controls (si-Ctrl; $n = 4$). ALDOA, aldolase fructose-bisphosphate (A). LDHB, lactate dehydrogenase (B). PDK2, pyruvate dehydrogenase kinase 2. PFKM, phosphofructokinase. *$P < 0.05$ (versus si-Ctrl), Student *T* test.

MBNL2), quaking (QKI), the poly-pyrimidine tract binding proteins 1 and 2 (PTBP1 and PTBP2), and the CUGBP elav-like family members 1 and 2 (CELF1 and CELF2), which may operate independently of H3K36me3 [40,49–52].

Although information regarding the role of SETD2 during myogenesis is limited, one previous study reported that CRISPR/Cas9-based genomic silencing of SETD2 blocked proliferation and differentiation of myoblast cells [33]. We did not observe morphological defects during differentiation after knocking down SETD2, which may be due to the fact that in this study we depleted, but did not completely silence, SETD2 and H3K36me3. Therefore, our results indicate that low levels of SETD2 and H3K36me3 are sufficient to permit differentiation, in contrast with complete SETD2 knock out studies. The observation that SETD2 knock down did not block differentiation allowed us to identify transcriptional changes that respond to SETD2 expression levels and are not a secondary effect of alterations in differentiation programs.

The Warburg effect is a shift towards glycolysis and lactate production, which has emerged as a key factor in tumour cell proliferation [53]. Notably, increased glycolysis is extremely common in clear cell renal cell carcinoma (ccRCC), a context in which loss-of-function mutations in the *SETD2* gene are frequently observed (approximately 10% of primary tumours) [54–56]. In addition to metabolic reprogramming, activation of the hypoxia-inducible factor 1 (HIF-1) pathway is a hallmark of ccRCC [54]. Here, we observed the upregulation of genes involved in glycolysis and HIF-1 signalling as a result of SETD2 loss in myotubes (Fig. 8D,E). For example, ALDOA is a key enzyme in the glycolytic pathway (and a HIF1 target gene), converting fructose-1,6-bisphosphate into glycerol-3-phosphate and its overexpression is associated with poor prognosis in ccRCC patient samples (and increased cell proliferation and invasion in renal carcinoma cell lines) [57,58]. Our results show that ALDOA is upregulated at both the mRNA and protein level in the absence of SETD2. These observations raise the possibility that SETD2 loss could mediate metabolic reprogramming in ccRCC and may be particularly interesting as the exact function of SETD2 mutations in ccRCC remains elusive.

Adult skeletal muscle tissue composes 30–40% of body mass and is the largest metabolic organ system in humans [59]. During myogenesis, mitochondrial biogenesis increases, and, correspondingly, metabolism programs shift from primarily glycolysis to oxidative phosphorylation [60,61]. Presumably, increased oxidative phosphorylation provides a larger supply of ATP,

which is necessary for contraction of mature muscle. Our results suggest that SETD2 is important for this developmentally regulated metabolic reprogramming and that reduction in the levels of SETD2 expression could revert metabolic pathways in mature muscle cell towards glycolysis. For example, we found that SETD2 depletion resulted in the upregulation of several glycolytic enzymes (PFKM, ALDOA, LDHB, and PDK2) concomitant with an increase in intracellular pyruvate levels. Taken together, our findings expand on previous reports that suggest an interplay between metabolic programs, histone modifications, and gene expression during myogenesis [14,62,63].

Materials and methods

Cell culture

Murine C2C12 myoblasts were obtained from ATCC (Manassas, VA, USA, CRL-1772) and maintained in a humidified incubator at 37 °C under 5% CO_2. Undifferentiated myoblasts were cultured in growth medium consisting of Dulbecco's Modified Eagle Medium (DMEM), 10% fetal bovine serum (FBS), 2 mM glutamine, 100 units·mL^{-1} of penicillin, and 100 µg·mL^{-1} streptomycin. Myoblasts were regularly subcultured to maintain a confluency under 40%. After reaching 80–100% confluency, cells were washed with phosphate buffered saline (PBS) and differentiation was initiated by replacing growth media with media containing DMEM, 2% horse serum, 100 units·mL^{-1} of penicillin, and 100 µg·mL^{-1} streptomycin (known as differentiation media). Differentiation media was refreshed every 2 days.

si-RNA delivery

Undifferentiated myoblasts were plated in DMEM supplemented with 10% FBS and 2 mM glutamine (7×10^4 cells per well in 6-well plates). The following day, myoblasts were transfected with a nontargeting si-RNA (Dharmacon, Lafayette, CO, USA, D-001210-01-20), si-Setd2 #1 (Dharmacon, D-062392-18), or si-Setd#2 (Dharmacon, D-062392-20) using the Lipofectamine RNAiMax transfection reagent (Invitrogen, Waltham, MA, USA, #13778075) according to the manufacturer's protocol. The next day, RNA and protein were collected from undifferentiated cells, or differentiation was initiated. RNA and protein were harvested after 4 days of differentiation.

RNA extraction

Cells were washed with PBS and RNA was extracted using TRIzol reagent (Invitrogen; RT-PCR and qPCR assays) or using the RNeasy mini kit (QIAGEN, Germantown, MD, USA, #74104) (RNA-sequencing studies). A NanoDrop

Lite Spectrophotometer (Thermo Fisher Scientific, Waltham, MA, USA, ND-LITE) was used to determine total RNA concentration.

RNA-sequencing

RNA quality was assessed using an HTX Synergy plate reader (BioTek, Winooski, VT, USA) with the Take3 micro-volume plate accessory (BioTek) and electrophoresis on a TapeStation instrument (Agilent, Santa Clara, CA, USA). All samples passed the following conditions: (a) $A_{260\,nm}/A_{280\,nm} \geq 1.9$, (b) $A_{260\,nm}/A_{230\,nm} \geq 1.6$, (c) DV200 $\geq$ 96, and (d) RNA integrated number (RIN) $\geq$ 8.5. Polyadenylated RNAs were captured, and cDNA libraries were generated using the KAPA stranded mRNA-Seq kit with KAPA mRNA capture beads (Roche, Basel, Switzerland, #07962207001). Final library quality and pool balance were determined using a MiSeq Nano instrument. Samples were pooled and analysed using an Illumina NovaSeq6000 instrument S4 flow-cell with 100 bp paired end reads.

RNA-sequencing analysis

Three independent replicates for all treatment conditions were generated for RNA-sequencing analysis. RNA-sequencing reads were aligned to the mouse genome (mm10) using STAR 2.7.6a [64]. Read counts were determined using salmon 1.4.0 [65]. Differential gene expression analysis was performed using the DESeq2 package [66] in R Studio. To exclude lowly expressed genes, those with less than 500 reads

P-values reported here were based on Fisher's exact test as determined by enrichr software [42–44].

Alternative splicing evaluation by RT-PCR

Reverse transcription of RNA into cDNA was performed using the high-capacity cDNA reverse transcription kit (Applied Biosystems, Waltham, MA, USA, #4368813) and RNase inhibitors (Applied Biosystems, N8080119). The following thermocycling conditions were used for reverse transcription: (a) 25 °C for 10 min, (b) 37 °C for 120 min, (c) 85 °C for 5 min, and (d) 4 °C pause. Alternative splicing primers were designed to hybridize with constitutive exons flanking the alternatively spliced regions using the UCSC genome browser and Primer 3 (Table S2). PCR assays were performed using GoTaq reagent (Promega, Madison, WI, USA, M7123) and primers diluted to a final concentration of 0.5 μM. Thermocycling conditions for PCR assays were as follows: (a) 95 °C for 1 min 15 s, (b) 28 cycles of 95 °C for 45 s, 57 °C for 45 s, 72 °C for 1 min, (c) 72 °C for 10 min, and (d) 4 °C pause. PCR products were separated using 6% polyacrylamide gel electrophoresis in TAE buffer (40 mM Tris, 20 mM acetic acid, 1 mM EDTA) at 140 V for 1–4 h. An ethidium bromide solution (0.4 μg·mL^{-1}) was used to stain gels for 10 min prior to imaging on the ChemiDocTM XRS+ imaging system (BioRad, Hercules, CA, USA). Densitometry quantifications were performed using the Image labTM 6.0.1 software (BioRad). Ethidium bromide oligo-length dependent staining bias was corrected using a standard curve and a pUC19 ladder. The PSI was determined by the following equation:

$$\text{PSI} = \frac{\text{Density of band including the alternative region}}{\text{Density of band including the alternative region} + \text{Density of band without the alternative region}}$$

total across all samples were removed. Genes with FC > 1.25 (which means FC > 1.25 for upregulation or FC < 1/1.25 for downregulation) and $P_{adjusted}$ < 0.05 were considered differentially expressed. Splicing analysis was performed using rmats 4.1.0 [67]. Differences in percent spliced in (ΔPSI) were calculated by subtracting the PSI following SETD2 depletion from the PSI under control conditions (i.e., si-Ctrl – si-Setd2). Splicing events with |ΔPSI| > 5%, P < 0.05, and FDR < 0.2 for both si-Setd2 #1 and si-Setd2 #2 were considered differentially spliced.

Gene ontology analysis

Differentially expressed genes were analysed using enrichr [42–44]. Data presented here were derived from analysis of 'Biological Process 2021' and 'KEGG 2021' pathways.

Real time quantitative PCR (qPCR)

mRNA expression levels were determined using Taqman Fast Advance Master Mix (Applied Biosystems), 50 ng input cDNA, and TaqMan probes (Table S3). Samples were analysed using an Applied Biosystems QuantStudio 7 Flex Real-Time PCR system with the following thermocycling program: (a) 95 °C for 20 s and (b) 40 cycles of 95 °C for 1 s, 60 °C for 20 s. Cycle threshold values of quantified transcripts were normalized to the cycle threshold of the hydroxymethylbilane synthase (Hmbs) control gene from the same sample.

Protein lysate preparation

After washing cells with ice cold PBS, ice cold RIPA lysis buffer (50 mM Tris, 150 mM NaCl, 1% Triton X-100, 0.5% sodium deoxycholate, 0.1% sodium dodecyl sulfate (SDS),

pH 7.5) containing protease and phosphatase inhibitors (Thermo Fisher Scientific) was used to lyse cells. Samples were immediately transferred to ice and incubated for 15 min before being sonicated in an ice bath at 75 V for 3 min (30 s on, 30 s off). Lysates were then incubated on ice for 15 min and centrifuged for 10 min at 18,000 g. at 4 °C. Supernatants containing the protein fraction were transferred to new tubes and protein concentration was estimated using the BCA protein assay kit (Thermo Fisher Scientific, #23225) according to manufacturer's instructions.

Western blotting

Protein samples were diluted in loading buffer (50 mM Tris–HCl pH 6.8, 12.5 mM EDTA, 10% glycerol, 2% SDS, 0.02% bromophenol blue, 360 mM beta-mercaptoethanol), boiled for 5 min, and resolved by SDS polyacrylamide gel electrophoresis (SDS/PAGE) in Mini-PROTEAN vertical electrophoresis systems (BioRad). Electrophoresis was performed at 90 V for 30 min followed by 45 min at 130 V. TGX Stain-free gels were activated for 2.5 min using a Chemi-Doc™ XRS+ imaging system (BioRad). For most targets, proteins were transferred into Amersham Hybond Low Fluorescence 0.2 µm PVDF membranes (GE Healthcare Life Sciences, Piscataway, NJ, USA, #10600022) using the Mini Trans-Blot Cell system (BioRad) at 100 V for 1 h. For SETD2, blots were transferred at 40 V overnight at 4 °C. To determine total protein loaded, blot images were captured using a ChemiDoc™ XRS+ imaging system (BioRad). After transfer, membranes were blocked with a 5% nonfat dry milk solution in tris-buffered saline with tween (TBST; 20 mM Tris-base, 137 mM NaCl, 0.1% tween 20, pH 7.6) for 1 h at room temperature, rinsed with TBST, and incubated overnight at 4 °C with primary antibodies diluted in 1% BSA in TBST: anti-SETD2 from Cell Signalling (Danvers, MA, USA, #23486; 1 : 500), anti-Histone H3 from Abcam (Cambridge, United Kingdom, ab1791; 1 : 1000), anti-H3K36me3 (a generous gift from Dr Brian Strahl at The University of North Carolina at Chapel Hill; 1 : 4000), anti-PFK1 from Santa Cruz Biotechnology (sc-377 346; 1 : 500), anti-ALDOA from Santa Cruz Biotechnology (Dallas, TX, USA, sc-390 733; 1 : 500), anti-PDK2 from Santa Cruz Biotechnology (sc-517 284; 1 : 500), anti-LDHB from Santa Cruz Biotechnology (sc-100 775; 1 : 500), anti-MYH from Santa Cruz Biotechnology (sc-376 157; 1 : 500), anti-MYOD1 from Santa Cruz Biotechnology (sc-377 460; 1 : 500), and anti-MYOG from Santa Cruz Biotechnology (sc-12 732; 1 : 500). The following day, primary antibody solutions were removed, and membranes were washed with TBST three times, for 10 min each. After the final wash, membranes were incubated with an anti-rabbit Dylight 800 secondary antibody (Thermo Fisher Scientific, SA5-35571) or anti-mouse Dylight 800 secondary antibody (Thermo Fisher Scientific, SA5-10176) diluted (1 : 10 000) in 1% BSA in TBST for 1 h in the darkness at room temperature. Membranes were then washed with TBST

three times (for 10 min each), imaged using an Odyssey Licor Imager and quantified using IMAGEJ [68]. H3K36me3 was normalized to total histone 3 (H3) from the same sample. All other target signals were normalized to total protein.

Intracellular pyruvate quantification

Pyruvate was measured with the Pyruvate Assay Kit from Abcam (ab65342) according to manufacturer's instructions. Briefly, transfected cells were harvested in assay buffer and treated with a master mix containing pyruvate oxidase which generated a fluorescent signal (excitation/emission = 535/587 nm) directly proportional to pyruvate levels. To prevent the conversion of pyruvate to lactate, samples were deproteinized using a 10 kDa cutoff spin filter (Pierce 88 513). Pyruvate content was calculated according to a standard curve generated from kit reagents. Data were normalized based on the average of four replicates of control (si-Ctrl) cells.

Immunofluorescence confocal microscopy and image processing

Cells were fixed with 4% paraformaldehyde diluted in PBS for 20 min at room temperature. Next, cells were washed three times in PBS, for 10 min each and incubated in blocking solution (1% BSA, 0.3% Triton in PBS) for 1 h, all at room temperature. Samples were incubated overnight at 4 °C with anti-MYH from Santa Cruz Biotechnology (sc-376 157; 1 : 150) diluted in blocking solution. The following day, cells were washed three times in PBS, for 10 min each before incubation with goat antimouse IgG (H + L) Alexa Fluor 488 from Thermo Fisher Scientific (A-11001; 1 : 150) diluted in blocking solution for 1 h at room temperature. Samples were washed three times in PBS, for 10 min each, incubated with 2 µM DAPI diluted in PBS for 5 min, and washed three additional times in PBS, all at room temperature. Images were captured at room temperature using a Zeiss 880 confocal microscope equipped with a Plan-Apo 10× objective (NA = 0.45, working distance = 2.0 mm) and ZEN BLACK (Zeiss, Oberkochen, Germany) image acquisition software. The following excitation parameters were used argon multiline laser at 488 nm (Alexa Fluor 488), or a 405 nm laser diode (DAPI). The following emission filters were used: band-pass 490–615 nm (Alexa Fluor 488) and band pass 410–514 nm (DAPI). Processing of images was performed using the FIJI software. Fusion index was determined as the percent of nuclei within MYH-positive myotubes with three or more nuclei.

Light microscopy and image processing

Live cells were imaged on an Olympus (Shinjuku City, Japan) IX83 microscope fitted with a 4× objective with a

Hamamatsu (Bridgewater, NJ, USA) C11440 camera and CELLSENS (Olympus, The Hague, The Netherlands) Dimension software. Processing of images was performed using the FIJI software [69].

Statistical analysis

Data are reported as mean ± SEM. An unpaired Student's *t*-test (two-tailed) was used to determine *P*-values, with those less than 0.05 considered statistically significant. The exceptions to this approach were the analyses of correlation, which relied on a *T* distribution under the null hypothesis of Pearson (ρ) = 0 and the analyses of overlap between differential gene expression or splicing under si-Setd2 #1 and si-Setd2 #2 treatment which was determined by a Fisher's exact test.

Acknowledgements

Conflict of interest

The authors declare no conflict of interest.

Author contributions

Data availability statement

All relevant data for this study are included in this published article and supporting information in the form of graphs.

All raw RNA-seq data files are available for download from NCBI Gene Expression Omnibus (http://www.ncbi.nlm.nih.gov/geo/) under accession number GSE199256. The full RNA-sequencing analysis results are available in File S1.

References

1 Butler JS, Koutelou E, Schibler AC, Dent SYR. Histone-modifying enzymes: regulators of developmental decisions and drivers of human disease. *Epigenomics*. 2012;**4**:163–77.

2 Bentzinger CF, Wang YX, Rudnicki MA. Building muscle: molecular regulation of myogenesis. *Cold Spring Harb Perspect Biol*. 2012;**4**:a008342.

3 Sincennes M-C, Brun CE, Rudnicki MA. Concise review: epigenetic regulation of myogenesis in health and disease. *Stem Cells Transl Med*. 2016;**5**:282–90.

4 Relaix F, Montarras D, Zaffran S, Gayraud-Morel B, Rocancourt D, Tajbakhsh S, et al. Pax3 and Pax7 have distinct and overlapping functions in adult muscle progenitor cells. *J Cell Biol*. 2006;**172**:91–102.

5 Kawakami K, Sato S, Ozaki H, Ikeda K. Six family genes – structure and function as transcription factors and their roles in development. *Bioessays*. 2000;**22**:616–26.

6 Gossett LA, Kelvin DJ, Sternberg EA, Olson EN. A new myocyte-specific enhancer-binding factor that recognizes a conserved element associated with multiple muscle-specific genes. *Mol Cell Biol*. 1989;**9**:5022–33.

7 Buskin JN, Hauschka SD. Identification of a myocyte nuclear factor that binds to the muscle-specific enhancer of the mouse muscle creatine kinase gene. *Mol Cell Biol*. 1989;**9**:2627–40.

8 Chen JF, Tao Y, Li J, Deng Z, Yan Z, Xiao X, et al. microRNA-1 and microRNA-206 regulate skeletal muscle satellite cell proliferation and differentiation by repressing Pax7. *J Cell Biol*. 2010;**190**:867–79.

9 Hirai H, Verma M, Watanabe S, Tastad C, Asakura Y, Asakura A. MyoD regulates apoptosis of myoblasts

through microRNA-mediated down-regulation of Pax3. *J Cell Biol.* 2010;**191**:347–65.

10 Mal A, Sturniolo M, Schiltz RL, Ghosh MK, Harter ML. A role for histone deacetylase HDAC1 in modulating the transcriptional activity of MyoD: inhibition of the myogenic program. *EMBO J.* 2001;**20**:1739–53.

11 Sartorelli V, Puri PL, Hamamori Y, Ogryzko V, Chung G, Nakatani Y, et al. Acetylation of MyoD directed by PCAF is necessary for the execution of the muscle program. *Mol Cell.* 1999;**4**:725–34.

12 Cao Y, Yao Z, Sarkar D, Lawrence M, Sanchez GJ, Parker MH, et al. Genome-wide MyoD binding in skeletal muscle cells: a potential for broad cellular reprogramming. *Dev Cell.* 2010;**18**:662–74.

13 Asp P, Blum R, Vethantham V, Parisi F, Micsinai M, Cheng J, et al. Genome-wide remodeling of the epigenetic landscape during myogenic differentiation. *Proc Natl Acad Sci USA.* 2011;**108**:149–58.

14 Yucel N, Wang YX, Mai T, Porpiglia E, Lund PJ, Markov G, et al. Glucose metabolism drives histone acetylation landscape transitions that dictate muscle stem cell function. *Cell Rep.* 2019;**27**:3939–55.e6.

15 McKinnell IW, Ishibashi J, Le Grand F, Punch VGJ, Addicks GC, Greenblatt JF, et al. Pax7 activates myogenic genes by recruitment of a histone methyltransferase complex. *Nat Cell Biol.* 2008;**10**:77–84.

16 Palacios D, Mozzetta C, Consalvi S, Caretti G, Saccone V, Proserpio V, et al. TNF/p38α/polycomb signaling to Pax7 locus in satellite cells links inflammation to the epigenetic control of muscle regeneration. *Cell Stem Cell.* 2010;**7**:455–69.

17 Caretti G, Di Padova M, Micales B, Lyons GE, Sartorelli V. The Polycomb Ezh2 methyltransferase regulates muscle gene expression and skeletal muscle differentiation. *Genes Dev.* 2004;**18**:2627–38.

18 Seenundun S, Rampalli S, Liu QC, Aziz A, Palii C, Hong S, et al. UTX mediates demethylation of H3K27me3 at muscle-specific genes during myogenesis. *EMBO J.* 2010;**29**:1401–11.

19 Verrier L, Escaffit F, Chailleux C, Trouche D, Vandromme M. A new isoform of the histone demethylase JMJD2A/KDM4A is required for skeletal muscle differentiation. *PLoS Genet.* 2011;**7**:e1001390.

20 Strahl BD, Grant PA, Briggs SD, Sun Z-W, Bone JR, Caldwell JA, et al. Set2 is a nucleosomal histone H3-selective methyltransferase that mediates transcriptional repression. *Mol Cell Biol.* 2002;**22**:1298–306.

21 Kolasinska-Zwierz P, Down T, Latorre I, Liu T, Liu XS, Ahringer J. Differential chromatin marking of introns and expressed exons by H3K36me3. *Nat Genet.* 2009;**41**:376–81.

22 Andersson R, Enroth S, Rada-Iglesias A, Wadelius C, Komorowski J. Nucleosomes are well positioned in exons and carry characteristic histone modifications. *Genome Res.* 2009;**19**:1732–41.

23 Xiao T, Hall H, Kizer KO, Shibata Y, Hall MC, Borchers CH, et al. Phosphorylation of RNA polymerase II CTD regulates H3 methylation in yeast. *Genes Dev.* 2003;**17**:654–63.

24 Bhattacharya S, Levy MJ, Zhang N, Li H, Florens L, Washburn MP, et al. The methyltransferase SETD2 couples transcription and splicing by engaging mRNA processing factors through its SHI domain. *Nat Commun.* 2021;**12**:1443.

25 Xie L, Pelz C, Wang W, Bashar A, Varlamova O, Shadle S, et al. KDM5B regulates embryonic stem cell self-renewal and represses cryptic intragenic transcription. *EMBO J.* 2011;**30**:1473–84.

26 Carrozza MJ, Li B, Florens L, Suganuma T, Swanson SK, Lee KK, et al. Histone H3 methylation by Set2 directs deacetylation of coding regions by Rpd3S to suppress spurious intragenic transcription. *Cell.* 2005;**123**:581–92.

27 Joshi AA, Struhl K. Eaf3 chromodomain interaction with methylated H3-K36 links histone deacetylation to pol II elongation. *Mol Cell.* 2005;**20**:971–8.

28 Keogh MC, Kurdistani SK, Morris SA, Ahn SH, Podolny V, Collins SR, et al. Cotranscriptional set2 methylation of histone H3 lysine 36 recruits a repressive Rpd3 complex. *Cell.* 2005;**123**:593–605.

29 Luco RF, Pan Q, Tominaga K, Blencowe BJ, Pereira-Smith OM, Misteli T. Regulation of alternative splicing by histone modifications. *Science.* 2010;**327**:996–1000.

30 Pradeepa MM, Sutherland HG, Ule J, Grimes GR, Bickmore WA. Psip1/Ledgf p52 binds methylated histone H3K36 and splicing factors and contributes to the regulation of alternative splicing. *PLoS Genet.* 2012;**8**:e1002717.

31 Xu S-J, Lombroso SI, Fischer DK, Carpenter M, Marchione DM, Hamilton PJ, et al. Chromatin-mediated alternative splicing regulates cocaine reward behavior. *Neuron.* 2021;**109**:2943–66.e8.

32 Hu M, Sun XJ, Zhang YL, Kuang Y, Hu CQ, Wu WL, et al. Histone H3 lysine 36 methyltransferase Hypb/Setd2 is required for embryonic vascular remodeling. *Proc Natl Acad Sci USA.* 2010;**107**:2956–61.

33 Yi X, Tao Y, Lin X, Dai Y, Yang T, Yue X, et al. Histone methyltransferase Setd2 is critical for the proliferation and differentiation of myoblasts. *Biochim Biophys Acta Mol Cell Res.* 2017;**1864**:697–707.

34 Yaffe D, Saxel O. Serial passaging and differentiation of myogenic cells isolated from dystrophic mouse muscle. *Nature.* 1977;**270**:725–7.

35 Blau HM, Pavlath GK, Hardeman EC, Chiu CP, Silberstein L, Webster SG, et al. Plasticity of the differentiated state. *Science.* 1985;**230**:758–66.

36 Montano M. Model systems. Translational biology in medicine. Sawston, Cambridge: Woodhead Publishing; 2014. p. 9–33.

37 Bland CS, Wang ET, Vu A, David MP, Castle JC, Johnson JM, et al. Global regulation of alternative splicing during myogenic differentiation. *Nucleic Acids Res*. 2010;**38**:7651–64.

38 Brinegar AE, Xia Z, Loehr JA, Li W, Rodney GG, Cooper TA. Extensive alternative splicing transitions during postnatal skeletal muscle development are required for Ca 2+ handling. *eLife*. 2017;**6**:e27192.

39 Hinkle ER, Wiedner HJ, Torres EV, Jackson M, Black AJ, Blue R, et al. Alternative splicing regulation of membrane trafficking genes during myogenesis. *RNA*. 2022;**28**:523–40.

40 Singh RK, Xia Z, Bland CS, Kalsotra A, Scavuzzo MA, Curk T, et al. Rbfox2-coordinated alternative splicing of Mef2d and Rock2 controls myoblast fusion during myogenesis. *Mol Cell*. 2014;**55**:592–603.

41 Millay DP, O'Rourke JR, Sutherland LB, Bezprozvannaya S, Shelton JM, Bassel-Duby R, et al. Myomaker is a membrane activator of myoblast fusion and muscle formation. *Nature*. 2013; **499**:301–5.

42 Chen EY, Tan CM, Kou Y, Duan Q, Wang Z, Meirelles GV, et al. Enrichr: interactive and collaborative HTML5 gene list enrichment analysis tool. *BMC Bioinformatics*. 2013;**14**:128.

43 Kuleshov MV, Jones MR, Rouillard AD, Fernandez NF, Duan Q, Wang Z, et al. Enrichr: a comprehensive gene set enrichment analysis web server 2016 update. *Nucleic Acids Res*. 2016;**44**:W90–7.

44 Xie Z, Bailey A, Kuleshov MV, Clarke DJB, Evangelista JE, Jenkins SL, et al. Gene set knowledge discovery with Enrichr. *Curr Protoc*. 2021;**1**:e90.

45 Skucha A, Ebner J, Schmöllerl J, Roth M, Eder T, César-Razquin A, et al. MLL-fusion-driven leukemia requires SETD2 to safeguard genomic integrity. *Nat Commun*. 2018;**9**:1983.

46 Xie P, Tian C, An L, Nie J, Lu K, Xing G, et al. Histone methyltransferase protein SETD2 interacts with p53 and selectively regulates its downstream genes. *Cell Signal*. 2008;**20**:1671–8.

47 Leung CS, Douglass SM, Morselli M, Obusan MB, Pavlyukov MS, Pellegrini M, et al. H3K36 methylation and the chromodomain protein Eaf3 are required for proper cotranscriptional spliceosome assembly. *Cell Rep*. 2019;**27**:3760–9.e4.

48 Pajoro A, Severing E, Angenent GC, Immink RGH. Histone H3 lysine 36 methylation affects temperature-induced alternative splicing and flowering in plants. *Genome Biol*. 2017;**18**:102.

49 Wang ET, Ward AJ, Cherone JM, Giudice J, Wang TT, Treacy DJ, et al. Antagonistic regulation of mRNA expression and splicing by CELF and MBNL proteins. *Genome Res*. 2015;**25**:858–71.

50 Hall MP, Nagel RJ, Fagg WS, Shiue L, Cline MS, Perriman RJ, et al. Quaking and PTB control overlapping splicing regulatory networks during muscle cell differentiation. *RNA*. 2013;**19**:627–38.

51 Batra R, Charizanis K, Manchanda M, Mohan A, Li M, Finn DJ, et al. Loss of MBNL leads to disruption of developmentally regulated alternative polyadenylation in RNA-mediated disease. *Mol Cell*. 2014;**56**:311–22.

52 Giudice J, Xia Z, Wang ET, Scavuzzo MA, Ward AJ, Kalsotra A, et al. Alternative splicing regulates vesicular trafficking genes in cardiomyocytes during postnatal heart development. *Nat Commun*. 2014;**5**:3603.

53 Liberti MV, Locasale JW. The Warburg effect: how does it benefit cancer cells? *Trends Biochem Sci*. 2016;**41**:211–8.

54 Wettersten HI, Aboud OA, Lara PN, Weiss RH. Metabolic reprogramming in clear cell renal cell carcinoma. *Nat Rev Nephrol*. 2017;**13**:410–9.

55 Hakimi AA, Ostrovnaya I, Reva B, Schultz N, Chen YB, Gonen M, et al. Adverse outcomes in clear cell renal cell carcinoma with mutations of 3p21 epigenetic regulators BAP1 and SETD2: A report by MSKCC and the KIRC TCGA research network. *Clin Cancer Res*. 2013;**19**:3259–67.

56 Creighton CJ, Morgan M, Gunaratne PH, Wheeler DA, Gibbs RA, Robertson G, et al. Comprehensivemolecular characterization of clear cell renal cell carcinoma. *Nature*. 2013;**499**:43–9.

57 Huang Z, Hua Y, Tian Y, Qin C, Qian J, Bao M, et al. High expression of fructose-bisphosphate aldolase A induces progression of renal cell carcinoma. *Oncol Rep*. 2018;**39**:2996–3006.

58 Na N, Li H, Xu C, Miao B, Hong L, Huang Z, et al. High expression of Aldolase A predicts poor survival in patients with clear-cell renal cell carcinoma. *Ther Clin Risk Manag*. 2017;**13**:279–85.

59 Janssen I, Heymsfield SB, Wang Z, Ross R. Skeletal muscle mass and distribution in 468 men and women aged 18–88 yr. *J Appl Physiol*. 2000;**89**:81–8.

60 Remels AHV, Langen RCJ, Schrauwen P, Schaart G, Schols AMWJ, Gosker HR. Regulation of mitochondrial biogenesis during myogenesis. *Mol Cell Endocrinol*. 2010;**315**:113–20.

61 Ryall JG, Cliff T, Dalton S, Sartorelli V. Metabolic reprogramming of stem cell epigenetics. *Cell Stem Cell*. 2015;**17**:651–62.

62 Anan K, Hino S, Shimizu N, Sakamoto A, Nagaoka K, Takase R, et al. LSD1 mediates metabolic reprogramming by glucocorticoids during myogenic differentiation. *Nucleic Acids Res*. 2018;**46**:5441–54.

63 Das S, Morvan F, Morozzi G, Jourde B, Minetti GC, Kahle P, et al. ATP citrate lyase regulates myofiber

differentiation and increases regeneration by altering histone acetylation. *Cell Rep.* 2017;**21**:3003–11.

64 Dobin A, Davis CA, Schlesinger F, Drenkow J, Zaleski C, Jha S, et al. STAR: Ultrafast universal RNA-seq aligner. *Bioinformatics*. 2013;**29**:15–21.

65 Patro R, Duggal G, Love MI, Irizarry RA, Kingsford C. Salmon provides fast and bias-aware quantification of transcript expression. *Nat Methods*. 2017;**14**:417–9.

66 Love MI, Huber W, Anders S. Moderated estimation of fold change and dispersion for RNA-seq data with DESeq2. *Genome Biol.* 2014;**15**:550.

67 Shen S, Park JW, Lu ZX, Lin L, Henry MD, Wu YN, et al. rMATS: Robust and flexible detection of differential alternative splicing from replicate RNA-Seq data. *Proc Natl Acad Sci USA.* 2014;**111**:E5593–601.

68 Schneider CA, Rasband WS, Eliceiri KW. NIH Image to ImageJ: 25 years of image analysis. *Nat. Methods*. 2012;**9**:671–675.

69 Rueden CT, Schindelin J, Hiner MC, DeZonia BE, Walter AE, Arena ET, et al. ImageJ2: ImageJ for the next generation of scientific image data. *BMC Bioinform.* 2017;**18**:529.

Supporting information

Additional supporting information may be found online in the Supporting Information section at the end of the article.

Table S1. RNA-sequence analysis alignment statistics (mm10) of SETD2 knockdown in myoblasts and myotubes using STAR 2.7.6a.

Table S2. Sequence of the primers (Thermo Fisher Scientific or Sigma) used for splicing validation by RT-PCR assays.

Table S3. TaqMan® probes (Applied Biosystems) used for real time quantitative PCR (qPCR) analysis.

File S1. RNA-sequencing analysis of SETD2-depleted myoblasts and myotubes.